International Journal of Minerals, Metallurgy and Materials
Volume 23, Number 2, February 2016, Page 176
DOI: 10.1007/s12613-016-1225-0

Corrosion behavior and characteristics of the product film of API X100 steel in acidic simulated soil solution

Cui-wei Du[1,2)], *Tian-liang Zhao*[1,2)], *Zhi-yong Liu*[1,2)], *Xiao-gang Li*[1,2)], *and Da-wei Zhang*[1,2)]

1) Corrosion and Protection Center, University of Science and Technology Beijing, Beijing 100083, China

2) Key Laboratory of Chinese Ministry of Education for Corrosion and Prevention, University of Science and Technology Beijing, Beijing 100083, China

(Received: 18 June 2015; revised: 26 August 2015; accepted: 1 September 2015)

Abstract: The short-term corrosion behavior of API X100 steel in an acidic simulated soil was investigated by electrochemical measurements and soaking experiments, followed by corrosion morphology observations and X-ray photoelectron spectroscopy analyses. The results show that X100 steel exhibits an obvious pitting susceptibility in an acidic soil environment. Pits nucleate after approximately 10 h of immersion. Along with the nucleation and growth of the pits, the charge-transfer resistance and open-circuit potential first increase sharply, then decrease slowly, and eventually reach a steady state. The maxima of the charge-transfer resistance and open-circuit potential are attained at approximately 10 h. The evolution of the electrochemical process is confirmed by the analysis of the product film. The product film exhibits a porous and loose structure and could not protect the substrate well. The product film is primarily composed of ferrous carbonate and ferrous hydroxide ($Fe(OH)_2$). The concentration of $Fe(OH)_2$ in the product film increases from the inside to the outside layer.

Keywords: oil pipelines; steel corrosion; acidic environment; pitting corrosion; corrosion films

1. Introduction

API X100 pipeline steel, as a future alternative to X60, X70, and X80 pipeline steels, has been developed to satisfy more stringent requirements of transportation efficiency and operational reliability against harsh environments [1–3]. X100 pipeline steel (hereinafter referred to as X100) exhibits a yield strength of 690 MPa and a tensile strain capacity of 142% in the longitudinal direction [4]. In view of its outstanding mechanical performance, X100 clearly has broad application prospects [5–6]. Furthermore, it has previously been practically installed in some locations [7–8].

As X100 is being more widely applied, its corrosion behavior in service environments is attracting increasing attention. Numerous studies on the corrosion behavior of X100 in simulated soil solutions have been reported [9–25]. Most of these previous reports have indicated that the primary corrosion form is pitting corrosion. Mahdi *et al.* [16] discussed the effect of temperature and erosion on the pitting corrosion behavior of X100 steel in aqueous silica slurries containing bicarbonate and chloride ions. Pitting was observed at 35°C but not at 22°C, where the erosion rate was low or approximately zero. Gadala and Alfantazi [17] studied the electrochemical behavior of X100 in NS4 solution, which is a near-neutral and mildly alkaline-pH simulated soil solution. From their results, the corrosion rate of X100 decreased when the pH value increased from 5.4 to 9.0 because the sufficient bicarbonate promoted the steel passivation and the chloride/sulfate content prevented the stable passivation. Eliyan *et al.* [19–21] also reported that the corrosion rate of X100 exhibited a cathodic dependence on bicarbonate concentration and temperature. In their study, the corrosion rate first decreased with increasing bicarbonate concentration and temperature because of the interface passivation and subsequently increased because of the depassivation effect of chloride ions. In addition to the aforementioned studies, corrosion under the interaction of force and environment, such as stress corrosion and corrosion fatigue, has been extensively investigated in simulated soil solutions [3,14,18,24–27]. These studies elucidated corrosion behaviors and mechanisms under stress conditions. However, most of the experiments were conducted in alkaline, neutral,

Corresponding author: Zhi-yong Liu E-mail: liuzhiyong7804@126.com

or near- neutral pH solutions. Research into the corrosion of X100 in acidic simulated soil solution has not been reported. Moreover, the previous studies also failed to provide a clear description of the evolution of the corrosion behavior of X100 in simulated soil solution.

In the present work, the corrosion behavior of X100 in an acidic simulated soil solution over time was characterized by *in situ* electrochemical impedance spectroscopy (EIS), scanning electron microscopy (SEM), and X-ray photoelectron spectroscopy (XPS). A solution simulated the typical acidic soil environment in southern China was prepared as the experimental medium. The evolution of the steel short-term corrosion behavior and the characteristics of the product film are discussed.

2. Experimental

2.1. Materials and solutions

The X100 steel used in this work was investigated in the as-received condition. Its chemical composition is shown in Table 1. The sulfur and phosphorus contents were obtained by infrared absorption testing; the contents of other elements were obtained by inductively coupled plasma–atomic emission spectrometry. The results indicated that the steel was a low-carbon micro-alloyed steel. Trace amounts of Mo and Si imparted slight corrosion resistance. Fig. 1 shows the metallographic microstructure, which is composed primarily of ferrite and exiguous needle-like bainite. The yield strength, tensile strength, and elongation of the X100 used in this work were 700 MPa, 855 MPa, and 14.8%, respectively.

Table 1. Chemical composition of X100 steel wt%

C	Si	Mn	P	S	Mo	Fe
0.04	0.20	1.50	0.011	0.003	0.02	Balance

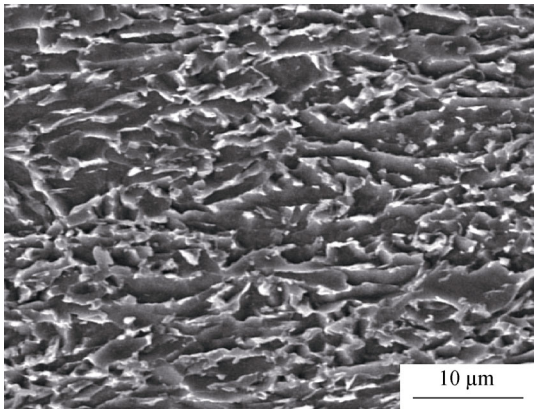

Fig. 1. Microstructure of X100 pipeline steel.

Test samples were machined into plates with dimensions of 10 mm × 10 mm × 3 mm. One of the 10 mm × 10 mm surfaces was welded to a copper wire for electrical contact. All the other surfaces were then coated with epoxy resin. The exposed surface was progressively ground with waterproof abrasive paper up to 1500 grit and then cleaned in an ultrasonic bath. Samples were dried with a blower and stored in a desiccator until used in experiments.

A simulated solution was prepared according to chemical analysis of the soil in Yingtan, which is typical of the acidic soil in most areas of southern China. The chemical composition of the solution is shown in Table 2. The pH value was modulated to approximately 4.5, which is the lower limit of the soil pH value. To simulate the oxygen-deficient underground environment, pure N_2 gas was blown into the solution for 2 h prior to each experiment. The system was then shielded from air by the addition of a suitable amount of liquid paraffin wax to the solution surface. All of the experiments were conducted at room temperature (approximately 23°C).

Table 2. Chemical composition of the simulated solution g/L

$CaCl_2$	NaCl	Na_2SO_4	$MgSO_4·7H_2O$	KNO_3	$NaHCO_3$
0.22	0.94	0.28	0.40	0.58	0.30

2.2. Electrochemical analyses

The electrochemical analyses included open-circuit potential (OCP) monitoring and EIS measurements. All electrochemical measurements were conducted in a typical three-electrode system, which comprised an X100 sample as the working electrode (WE), a saturated calomel electrode (SCE) as the reference electrode (RE), and a platinum plate as the counter electrode (CE). All potential data were obtained vs. SCE. A Princeton Applied Research 2273 electrochemical workstation was used to acquire the data. Before the measurements, all samples were immersed in the simulated solution for 30 min to ensure that the working surface reached a steady state. For EIS measurements, the test frequency ranged from 10 kHz to 0.01 Hz, and the AC amplitude was 10 mV. For both OCP and EIS measurements, data were recorded at immersion times of 1, 2, 4, 10, 20, 33, 57, 80, and 122 h.

2.3. Immersion tests

To achieve an intuitive understanding of the corrosion behavior of X100, the immersion experiments were performed on two parallel samples. After immersion, the surface morphology of corrosion products on one of the paral-

lel samples was observed by SEM. The corrosion products were then removed using a descaling solution (500 mL HCl + 500 mL H_2O + 4 g hexamethylenetetramine). The surface morphology of the sample after the corrosion products were removed was also observed by SEM.

2.4. XPS analyses

The compositions of the product films on the other parallel sample were analyzed by XPS. Before the XPS analyses, the impurities adsorbed onto the surface of the outside layer were removed by vacuum sputtering for 10 min. The outside layer of the product film was then scanned over the full range and the single-element ranges. The surface layer was then slightly ground using 1000 and 1500 grit abrasive papers to expose the inside layer. The inside layer was cleaned with deionized water and acetone and then dried with a blower. The inside layer was scanned in the same manner as the outside layer.

3. Results

3.1. Electrochemical results

Fig. 2 shows the OCP variation of X100 as a function of immersion time. The OCP first increases sharply, then decreases slowly, and eventually becomes steady during the soaking time. The maximum OCP is reached at approximately 10 h.

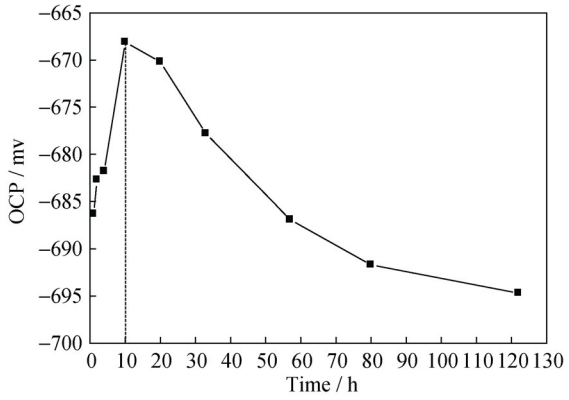

Fig. 2. OCP variation of X100 in acidic simulated soil solution as a function of immersion time.

The results of EIS measurements are shown in Fig. 3. From 0 to 4 h, the radius of the capacitive reactance arc increases with increasing immersion time, and an obvious inductive arc appears in the low-frequency region. From 4 h to 20 h, the inductive arc begins to disappear, and the radius of the capacitive arc tends to decrease. After 20 h, the inductive arc totally disappears, and the radius of the capacitive arc increases further.

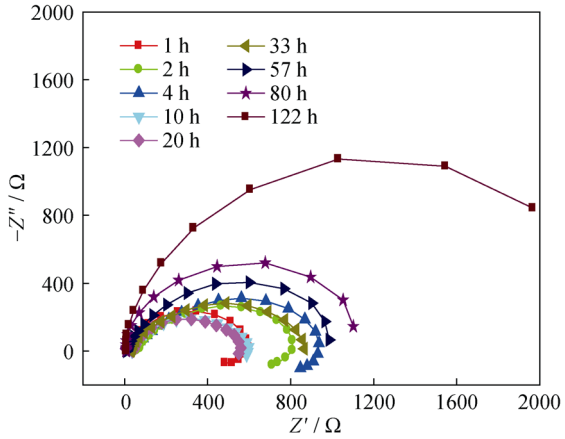

Fig. 3. Nyquist curves for X100 steel immersed in acidic simulated soil solution for different times.

3.2. Corrosion morphologies

The surface morphologies of X100 steel immersed for 10, 33, 57, and 122 h with the corrosion products removed are shown in Fig. 4. After 10 h of immersion, the shallow corrosion spots appear on the surface, as shown in Fig. 4(a). After 33 h, these spots are deepened and pits are observed to nucleate in Fig. 4(b). After 57 h, as shown Figs. 4(c) and (d), the number of pitting holes obviously increases during the soaking time. Fig. 5 shows the surface morphology of corrosion products after the specimen being soaked for 122 h. A porous and loose product film is formed on the surface.

3.3. Composition of the product film

The compositions of the outside and inside layers of the product film were investigated by XPS. Fig. 6 shows the full XPS spectrum of the product film; this spectrum indicates that oxygen, iron, and carbon are the main elements in the product film. Thus, the film is consisted primarily of carbonates and oxides of iron. A comparison of Fig. 6(a) and Fig. 6(b) revealed that the contents of oxygen and iron in the inside layer were greater than those in the outside layer and that the content of carbon in the inside layer was lesser than that in the outside layer. These differences in composition between the inside and outside layers may be related to the evolutionary process of the product layer.

Fig. 7 is the XPS spectra of iron and carbon, in the product film. The product film consists mainly of bivalent iron (Fe^{2+}, peaks at approximately 708.6 eV) and carbonate or bicarbonate (CO_3^{2-} or HCO_3^-, peaks at approximately 289.0 eV) in the product film. The organic carbon (peaks at approximately 285.0 eV in Fig. 7(b)) may originate from the unexpected pollution.

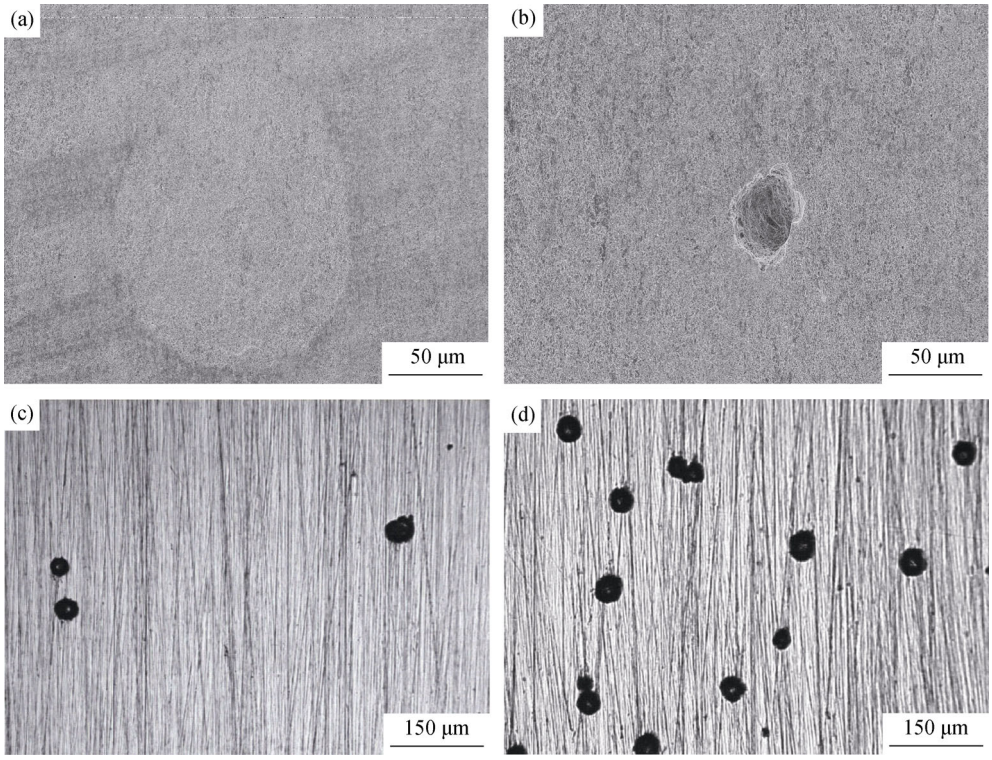

Fig. 4. Surface morphologies of X100 samples immersed in acidic simulated soil solution with the corrosion products removed: (a) 10 h; (b) 33 h; (c) 57 h; (d) 122 h.

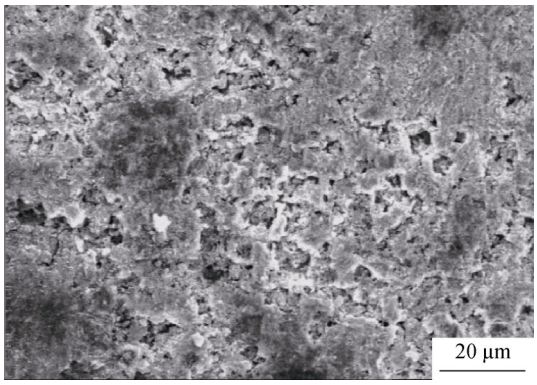

Fig. 5. Morphology of the product film of X100 after immersion in acidic simulated soil solution for 122 h.

The XPS spectra of oxygen (O 1s) in the inside and outside layers of the product film are shown in Fig. 8. The spectra show that oxygen is present in two primary states: as carbonate or bicarbonate (CO_3^{2-} or HCO_3^-, peaks at approximately 531.8 eV) and hydroxyl (OH^-, peaks at approximately 530.1 eV). Therefore, it was confirmed that the product film contained primarily ferrous carbonate ($FeCO_3$) and ferrous hydroxide ($Fe(OH)_2$). A comparison between Fig. 8(a) and Fig. 8(b) revealed that oxygen in the outside layer existed less in the form of OH^- and more in the form of CO_3^{2-} or HCO_3^- compared to oxygen in the inside layer; i.e., the concentration of $Fe(OH)_2$ in the product film tended to increase from the inside layer to the outside layer.

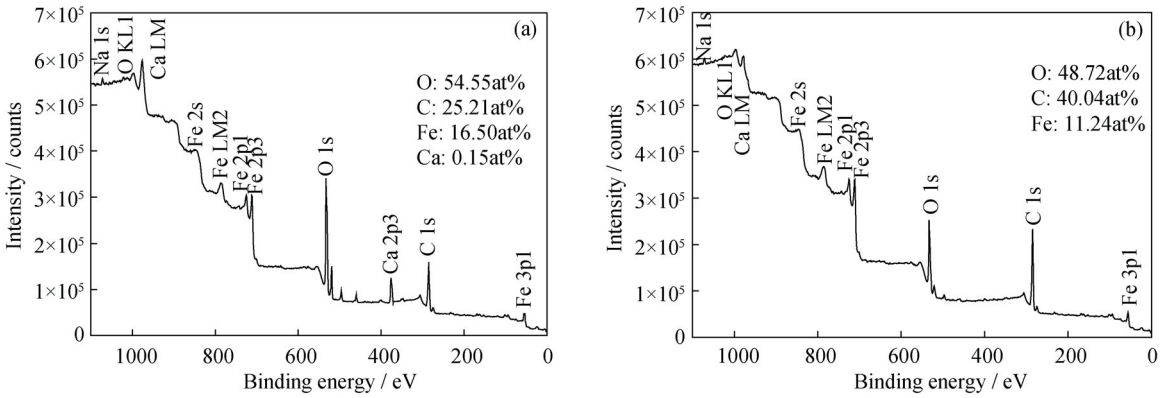

Fig. 6. Full XPS spectra of the inside layer (a) and the outside layer(b) of the product film after 122 h of immersion.

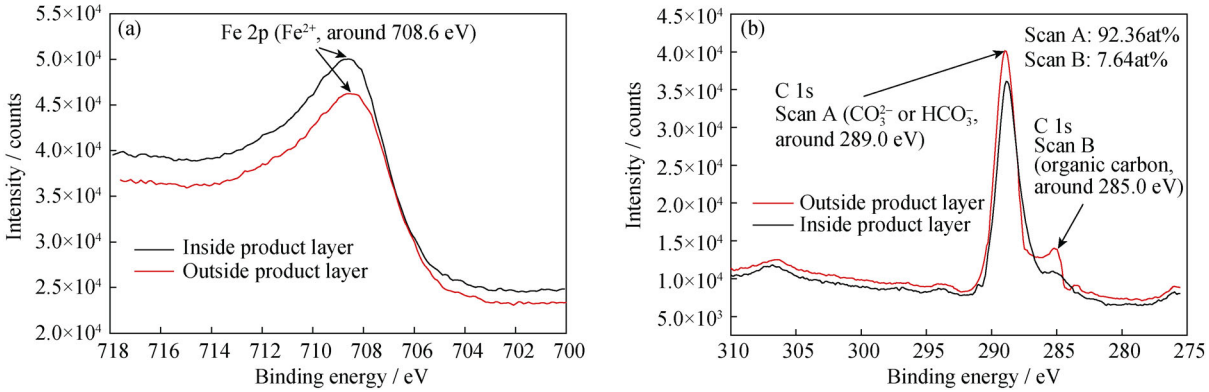

Fig. 7. XPS spectra of iron (a) and carbon (b) in the product film after 122 h of soaking.

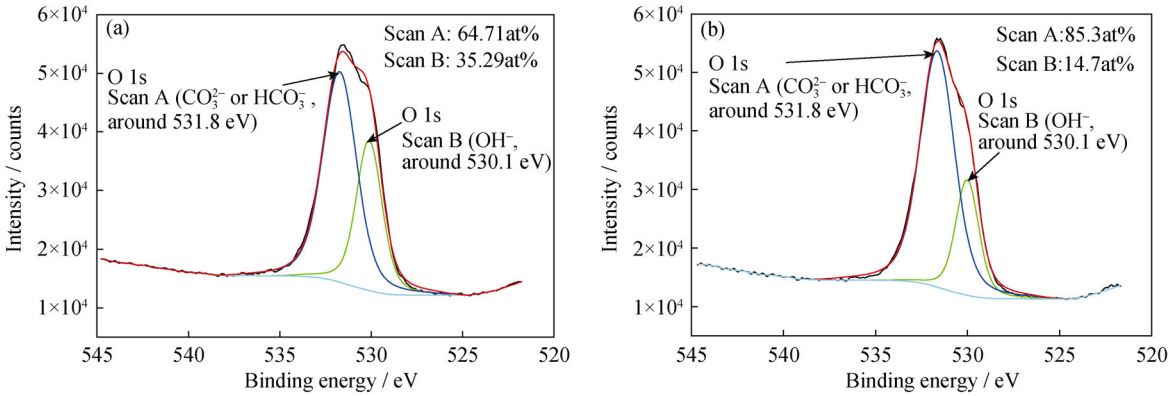

Fig. 8. XPS spectra of oxygen in the inside (a) and outside (b) layer after 122 h of immersion.

4. Discussion

The Nyquist curve constructed from EIS data for X100 during the initial 4 h showed an increasing interface resistance and the presence of an inductance arc in the low-frequency region. Generally, an inductance arc is related to the adsorption of electrochemically active products or the intermediate in the anodic dissolution reaction. According to Bockris *et al.* [28], the anodic dissolution of iron proceeds as the following equations.

$$Fe + H_2O = Fe(H_2O)_{ads} \quad (1)$$

$$Fe(H_2O)_{ads} = FeOH_{ads} + H^+ + e^- \quad (2)$$

$$FeOH_{ads} \rightarrow FeOH^+ + e^- \quad (3)$$

$$FeOH^+ + H^+ = Fe^{2+} + H_2O \quad (4)$$

where $Fe(H_2O)_{ads}$ and $FeOH_{ads}$ are the adsorption intermediates. The inductance arc during the initial 4 h is hypothesized to be caused by the adsorption of $Fe(H_2O)_{ads}$ and $FeOH_{ads}$. The total anodic reaction is expressed as Eq. (5).

$$Fe \rightarrow Fe^{2+} + 2e^- \quad (5)$$

Because the pH value of the simulated solution was approximately 4.0, HCO_3^- ions should have partly transformed into H_2CO_3 according to thermodynamic calculations [29]. Because the solution was deoxidized, the cathodic reaction could not be the reduction of oxygen. Moreover, Warburg impedance, which reflects the reduction of H^+, was not observed in the low-frequency region. Thus, the reduction of H^+ also could not be included in the cathodic reactions. Actually, in an acidic environment, the reduction of H_2CO_3 or HCO_3^- is thermodynamically more favorable than the reduction of H_2O [30]. The cathodic reaction process during the initial 4 h is represented as

$$H_2CO_3 + e^- \rightarrow HCO_3^- + H_{ads}, \quad (6)$$

$$HCO_3^- + e^- \rightarrow CO_3^{2-} + H_{ads}, \quad (7)$$

$$H_{ads} + H_{ads} \rightarrow H_2. \quad (8)$$

The corrosion products are presumed to be generated by the following reactions.

$$Fe^{2+} + 2HCO_3^- = FeCO_3(s) + H_2CO_3 \quad (9)$$

$$Fe^{2+} + CO_3^{2-} = FeCO_3(s) \quad (10)$$

$$Ca^{2+} + CO_3^{2-} = CaCO_3(s) \quad (11)$$

The production of $FeCO_3$ and $CaCO_3$ was confirmed by the

XPS results. $FeCO_3$ and some of $CaCO_3$ were directly deposited onto the sample surface. The initial products were compactly and tightly adhered to the substrate. A relatively steady product film gradually formed. Therefore, the OCP and the radius of the capacitive arc increased over time during the initial 4 h, as shown in Figs. 2 and 3. Simultaneously, as the film progressively covered more of the sample area, it gradually prevented the adsorption of $Fe(H_2O)_{ads}$ and $FeOH_{ads}$, resulting in the disappearance of the inductance arc at 10 h, as shown in Fig. 3.

When the soaking time reached 10 h, the sample surface was almost completely covered by the film. However, chloride ions could still penetrate into it. These ions made the sample surface unsteady, which resulted in the pitting nucleation. The OCP and interface resistance then decreased. After 20 h, Fe^{2+} ions generated by substrate dissolution in the pits diffused into the solution. When $[Fe^{2+}] \times [CO_3^{2-}]$ exceeded the solubility of $FeCO_3$, $FeCO_3$ was deposited, and a secondary film was formed on the previous film which exhibited a porous structure, as shown in Fig. 5. Simultaneously, the pitting holes deepened. The thickened film limited the diffusion of ions, which caused the interface resistance to increase again. As $FeCO_3$ continued to be deposited, H_2CO_3, HCO_3^-, and CO_3^{2-} species in the pit holes were exhausted. Therefore, Eqs. (9) and (10) should be replaced by the hydrolyzation of Fe^{2+} ions and $FeCO_3$ as follows:

$$Fe^{2+} + 2H_2O = Fe(OH)_2(s) + 2H^+, \quad (12)$$

$$FeCO_3(s) + 2H_2O = Fe(OH)_2(s) + H_2CO_3. \quad (13)$$

The generated $Fe(OH)_2$ in the pit holes preferentially deposited onto the inside of the product film. This process explained why the concentration of hydroxyl (OH^-) ions in the inside layer was greater than that in the outside layer (Fig. 8).

On the basis of the aforementioned analysis, the equivalent circuit models corresponding to different immersion durations were proposed, as shown in Fig. 9, where R_{sol} is the solution resistance, R_{pore} the solution resistance in the pitting holes, Q_{dl} the double-layer capacitance, R_{ct} the charge-transfer resistance, L and R_L the inductance and resistance induced by the dissolution of the product film, respectively, and Q_f the film inductance. Nyquist curves for samples soaked for different durations were fitted by the software ZSimpWin according to the corresponding equivalent circuit models. The conformity between the proposed circuits and some selected Nyquist curves are shown in Fig. 10.

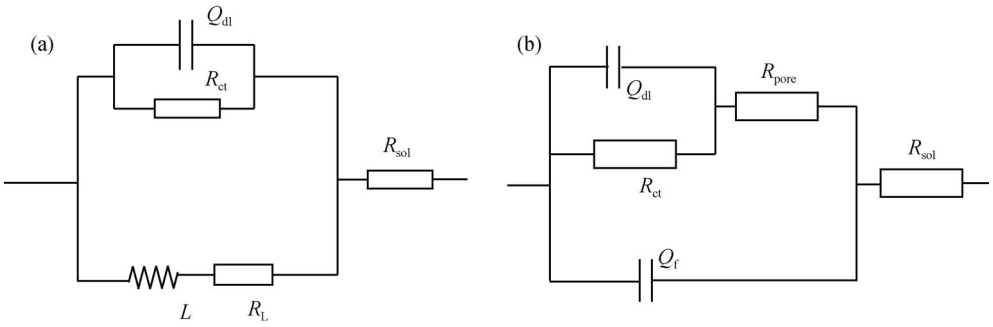

Fig. 9. Equivalent circuit models proposed for the electrochemical impedance responses before (a) and after (b) 20 h of immersion.

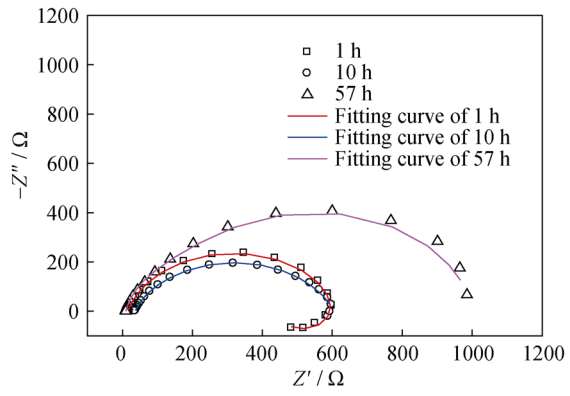

Fig. 10. Conformity between the proposed circuits and some selected Nyquist data.

The variation of the fitting value of R_{ct} with increasing immersion time is shown in Fig. 11. These results are consistent with the OCP trend in Fig. 2. R_{ct} is well known to primarily reflect the resistance of the interface reactions between substrate and solution. The sharp increase during the initial 10 h indicates that the interface reactions are blocked by the quick passivation. In the later immersion stage (after 33 h), the R_{ct} value decreases and eventually remains steady, consistent with the variation of the Nyquist curves after 33 h in Fig. 3. These results indicated that the interface reactions were activated by pitting although the thickness of the product film continued to increase.

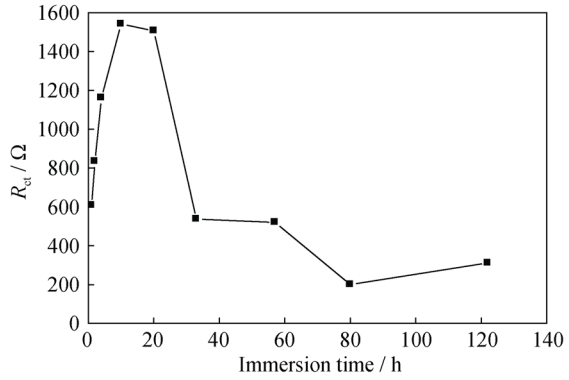

Fig. 11. Variation of charge-transfer resistance with immersion time.

5. Conclusions

(1) X100 steel exhibits an obvious pitting susceptibility in the acid soil environment. During the initial soaking time, a relatively steady product film forms on the surface. The film provides certain protective effect. However, pits nucleate after soaking the samples for approximately 10 h. Along with the nucleation and growth of these pits, the charge-transfer resistance and OCP first increase sharply, then decrease slowly, and eventually remain steady. Their maxima are both reached at approximately 10 h.

(2) The product film is mainly composed of $FeCO_3$ and $Fe(OH)_2$. Because of the consumption of CO_3^{2-} ions and the hydrolyzation of Fe^{2+} ions in pit holes during the soaking time, the concentration of $Fe(OH)_2$ in the product film exhibits an increase from the inside layer to the outside layer.

Acknowledgements

This work was financially supported by the National High-Tech Research and Development Program of China (No. 2012AA040105), the National Nature Science Foundation of China (Nos. 51131001 and 51741034), and the Beijing Higher Education Young Elite Teacher Project.

References

[1] Z.Y. Liu, X.G. Li, C.W. Du, L. Lu, Y.R. Zhang, and Y.F. Cheng, Effect of inclusions on initiation of stress corrosion cracks in X70 pipeline steel in an acidic soil environment, *Corros. Sci.*, 51(2009), No. 4, p. 895.

[2] M.A. Mohtadi-Bonab, J.A. Szpunar, and S.S. Razavi-Tousi, A comparative study of hydrogen induced cracking behavior in API 5L X60 and X70 pipeline steels, *Eng. Failure Anal.*, 33(2013), p. 163.

[3] L.W. Wang, X.H. Wang, Z.Y. Cui, Z.Y. Liu, C.W. Du, and X.G. Li, Effect of alternating voltage on corrosion of X80 and X100 steels in a chloride containing solution: investigated by AC voltammetry technique, *Corros. Sci.*, 86(2014), p. 213.

[4] R. Ghajar, G. Mirone, and A. Keshavarz, Ductile failure of X100 pipeline steel: experiments and fractography, *Mater. Des.*, 43(2013), p. 513.

[5] W.G. Zhao, M. Chen, S.H. Chen, and J.B. Qu, Static strain aging behavior of an X100 pipeline steel, *Mater. Sci. Eng. A*, 550(2012), p. 418.

[6] T.Y. Jin and Y.F. Cheng, *In situ* characterization by localized electrochemical impedance spectroscopy of the electrochemical activity of microscopic inclusions in an X100 steel, *Corros. Sci.*, 53(2011), No. 2, p. 850.

[7] M.A. Maes, M. Dann, and M.M. Salama, Influence of grade on the reliability of corroding pipelines, *Reliab. Eng. Syst. Saf.*, 93(2008), No. 3, p. 447.

[8] T.Y. Jin, Z.Y. Liu, and Y.F. Cheng, Effect of non-metallic inclusions on hydrogen-induced cracking of API5L X100 steel, *Int. J. Hydrogen Energy*, 35(2010), No. 15, p. 8014.

[9] S. Nafisi, M.A. Arafin, L. Collins, and J. Szpunar, Texture and mechanical properties of API X100 steel manufactured under various thermomechanical cycles, *Mater. Sci. Eng. A*, 531(2012), p. 2.

[10] C.F. Dong, Z.Y. Liu, X.G. Li, and Y.F. Cheng, Effects of hydrogen-charging on the susceptibility of X100 pipeline steel to hydrogen-induced cracking, *Int. J. Hydrogen Energy*, 34(2009), No. 24, p. 9879.

[11] B. Tanguy, T.T. Luu, G. Perrin, A. Pineau, and J. Besson, Plastic and damage behaviour of a high strength X100 pipeline steel: experiments and modelling, *Int. J. Pressure Vessels Piping*, 85(2008), No. 5, p. 322.

[12] F. Oikonomidis, A. Shterenlikht, and C.E. Truman, Prediction of crack propagation and arrest in X100 natural gas transmission pipelines with the strain rate dependent damage model (SRDD): Part 1. A novel specimen for the measurement of high strain rate fracture properties and validation of the SRDD model parameters, *Int. J. Pressure Vessels Piping*, 105-106(2013), p. 60.

[13] G. Mirone and D. Corallo, Stress–strain and ductile fracture characterization of an X100 anisotropic steel: Experiments and modelling, *Eng. Fract. Mech.*, 102(2013), p. 118.

[14] L.Y. Xu and Y.F. Cheng, Corrosion of X100 pipeline steel under plastic strain in a neutral pH bicarbonate solution, *Corros. Sci.*, 64(2012), p. 145.

[15] A. Mustapha, E.A. Charles, and D. Hardie, Evaluation of environment-assisted cracking susceptibility of a grade X100 pipeline steel, *Corros. Sci.*, 54(2012), p. 5.

[16] E. Mahdi, A. Rauf, and E.O. Eltai, Effect of temperature and erosion on pitting corrosion of X100 steel in aqueous silica slurries containing bicarbonate and chloride content, *Corros. Sci.*, 83(2014), p. 48.

[17] I.M. Gadala and A. Alfantazi, Electrochemical behavior of API-X100 pipeline steel in NS4, near-neutral, and mildly alkaline pH simulated soil solutions, *Corros. Sci.*, 82(2014), p. 45.

[18] L.Y. Xu and Y.F. Cheng, An experimental investigation of corrosion of X100 pipeline steel under uniaxial elastic stress in a near-neutral pH solution, *Corros. Sci.*, 59(2012), p. 103.

[19] F.F. Eliyan, F. Mohammadi, and A. Alfantazi, An electrochemical investigation on the effect of the chloride content on CO_2 corrosion of API-X100 steel, *Corros. Sci.*, 64(2012), p. 37.

[20] F.F. Eliyan, E.S. Mahdi, and A. Alfantazi, Electrochemical evaluation of the corrosion behaviour of API-X100 pipeline steel in aerated bicarbonate solutions, *Corros. Sci.*, 58(2012), p. 181.

[21] F.F. Eliyan and A. Alfantazi, Influence of temperature on the corrosion behavior of API-X100 pipeline steel in 1-bar CO_2–HCO_3^- solutions: An electrochemical study, *Mater. Chem. Phys.*, 140(2013), No. 2-3, p. 508.

[22] F.F. Eliyan and A. Alfantazi, Corrosion of the heat-affected zones (HAZs) of API-X100 pipeline steel in dilute bicarbonate solutions at 90°C: an electrochemical evaluation, *Corros. Sci.,* 74(2013), p. 297.

[23] F.F. Eliyan and A. Alfantazi, On the theory of CO_2 corrosion reactions: investigating their interrelation with the corrosion products and API-X100 steel microstructure, *Corros. Sci.*, 85(2014), p. 380.

[24] M. Al-Mansour, A.M. Alfantazi, and M. El-boujdaini, Sulfide stress cracking resistance of API-X100 high strength low alloy steel, *Mater. Des.*, 30(2009), No. 10, p. 4088.

[25] R.L. Amaro, N. Rustagi, K.O. Findley, E.S. Drexler, and A.J. Slifka, Modeling the fatigue crack growth of X100 pipeline steel in gaseous hydrogen, *Int. J. Fatigue*, 59(2014), p. 262.

[26] L. Fan, C.W. Du, Z.Y. Liu, and X.G. Li, Stress corrosion cracking of X80 pipeline steel exposed to high pH solutions with different concentrations of bicarbonate, *Int. J. Miner. Metall. Mater.*, 20(2013), No. 7, p. 645.

[27] D.J. Kong and C.D. Ye, Effects of laser heat treatment on the fracture morphologies of X80 pipeline steel welded joints by stress corrosion, *Int. J. Miner. Metall. Mater.*, 21(2014), No. 9, p. 898.

[28] J.O'M. Bockris, D. Drazic, and A.R. Despic, The electrode kinetics of the deposition and dissolution of iron, *Electrochim. Acta*, 4(1961), No. 2-4, p. 325.

[29] L.W. Liu, Q. Hu, J.X. Peng, and Z.Q. Yang, CO_2 corrosion of carbon steel in aqueous solution, *Mater. Prot.*, 34(2001), No. 1, p. 6.

[30] S. Nesic, J. Postlethwaite, and S. Olsen, An electrochemical model for prediction of corrosion of mild steel in aqueous carbon dioxide solutions, *Corros. Sci.*, 52(1996), No. 4, p. 280.